PHASED-ARRAY MONOLITHIC PEM FOR FT SPECTROMETRY WITH APPLICATIONS IN EXPLOSIVE DETECTION AND CB DEFENSE

Tudor N. Buican*
Semiotic Engineering Associates LLC
Albuquerque, NM 87108

Arthur H. Carrieri
US Army RDECOM Edgewood Chemical Biological Center (ECBC)
Aberdeen Proving Ground, MD 21010

ABSTRACT

We present the theory and multiphysics simulation of a novel type of photoelastic modulator (PEM) for use in ultra-high performance FT spectrometers with applications in the optical recognition of explosives and CB warfare agents. This new technology is based on the strain birefringence induced along a bar-shaped optical element by a phased array of piezoelectric transducers (PZT). Appropriate phase and amplitude relationships among the array PZTs ensure that induced birefringence oscillations add constructively and result in high total retardation. When used in PEM/FT spectrometers (Buican, 2006; Buican and Carrieri, 2004, 2006), monolithic virtual-stack/phased-array (VSPA) PEMs (Buican 2008) will provide ultra-high scan rates (to $>10^5$ interferograms/s); broad spectral range; high spectral resolution; and high light throughput.

1. INTRODUCTION

For historical reasons, commercial off-the-shelf (COTS) PEMs have been designed for low retardation amplitudes; as a consequence, higher resolution PEM/FT spectrometers must employ stacked PEMs (up to ten in one design) (Buican and Carrieri 2004). However, the very large number of optical surfaces in such a system results in significant light losses. We cut through the Gordian knot of the resolution-throughput compromise with a PEM devised specifically for high-resolution, high-throughput PEM/FT spectrometry. Such a PEM has a single bar-shaped optical element in lieu of a stack of conventional PEMs, with multiple PZTs attached to the bar at appropriate intervals. As light travels along the bar, local retardations add up to total values comparable to those for stacks of phase-locked individual PEMs. The bar-shaped PEM can thus be regarded as a virtual stack of conventional PEMs.

The difficulty with such a system is that elastic waves generated by individual PZTs propagate not only across the thickness of the bar but also along its length. As the associated stress and consequent birefringence change sign every half-wavelength of the longitudinally propagating elastic waves, the total retardation contributed by each PZT will oscillate rather than monotonically increase with increasing bar length. Furthermore, overlapping elastic waves generated by neighboring PZTs have differing phases, thus reducing the amplitude of the associated retardation. These factors tend to defeat the very purpose of the bar-shaped optical element and of the multiple PZTs attached to it.

We present in this paper a conceptual framework for solving the longitudinal propagation problem and understanding VSPA-PEM operation. This framework rests on the basic idea that elastic wave propagation along the axis of the bar can be confined through the use of "active mirrors" consisting of additional PZTs driven at appropriate amplitudes and phases. Furthermore, we show that a suitably driven phased array of PZTs placed along the PEM bar behaves like a stack of mechanically isolated conventional PEMs—hence the virtual-stack/phased array, or VSPA, name of the technology. Being isolated, these stacked "virtual" PEMs can be driven in phase and thus constructively contribute to a total retardation which is the scalar sum of the individual virtual PEM amplitudes.

Finally, we discuss the strategic advantage offered by VSPA-based PEM/FT as the enabling technology for several novel techniques for (i) the detection of trace amounts of explosives on surfaces; and (ii) the early warning of dangerous environmental CB threats evolving on the battlefield or in the homeland.

2. PEM/FT SPECTROMETRY BACKGROUND

PEM/FT spectrometers are based on birefringence interferometers, which introduce a variable retardation between interfering waves separated by their mutually orthogonal directions of polarization. The retardation is proportional to the instantaneous birefringence of the modulator and can be varied in time in order to scan an interferogram. PEM-based FT spectrometers cover broad spectral ranges (UV to NIR with fused silica optics, and NIR to mid-IR with ZnSe optics). In its simplest imple-

Report Documentation Page

Form Approved
OMB No. 0704-0188

Public reporting burden for the collection of information is estimated to average 1 hour per response, including the time for reviewing instructions, searching existing data sources, gathering and maintaining the data needed, and completing and reviewing the collection of information. Send comments regarding this burden estimate or any other aspect of this collection of information, including suggestions for reducing this burden, to Washington Headquarters Services, Directorate for Information Operations and Reports, 1215 Jefferson Davis Highway, Suite 1204, Arlington VA 22202-4302. Respondents should be aware that notwithstanding any other provision of law, no person shall be subject to a penalty for failing to comply with a collection of information if it does not display a currently valid OMB control number.

1. REPORT DATE	2. REPORT TYPE	3. DATES COVERED
01 DEC 2008	**N/A**	**-**

4. TITLE AND SUBTITLE **Phased-Array Monolithic PEM For FT Spectrometry With Applications In Explosive Detection And CB Defense**	5a. CONTRACT NUMBER 5b. GRANT NUMBER 5c. PROGRAM ELEMENT NUMBER
6. AUTHOR(S)	5d. PROJECT NUMBER 5e. TASK NUMBER 5f. WORK UNIT NUMBER
7. PERFORMING ORGANIZATION NAME(S) AND ADDRESS(ES) **Semiotic Engineering Associates LLC Albuquerque, NM 87108**	8. PERFORMING ORGANIZATION REPORT NUMBER
9. SPONSORING/MONITORING AGENCY NAME(S) AND ADDRESS(ES)	10. SPONSOR/MONITOR'S ACRONYM(S) 11. SPONSOR/MONITOR'S REPORT NUMBER(S)

12. DISTRIBUTION/AVAILABILITY STATEMENT
Approved for public release, distribution unlimited

13. SUPPLEMENTARY NOTES
See also ADM002187. Proceedings of the Army Science Conference (26th) Held in Orlando, Florida on 1-4 December 2008, The original document contains color images.

14. ABSTRACT

15. SUBJECT TERMS

16. SECURITY CLASSIFICATION OF:			17. LIMITATION OF ABSTRACT	18. NUMBER OF PAGES	19a. NAME OF RESPONSIBLE PERSON
a. REPORT	b. ABSTRACT	c. THIS PAGE			
unclassified	**unclassified**	**unclassified**	**UU**	**8**	

Standard Form 298 (Rev. 8-98)
Prescribed by ANSI Std Z39-18

mentation (Fig. 1a), a birefringence interferometer consists of a birefringent modulator placed between two polarizers (Buican and Martin, 1990). The optical axes of the birefringent modulator are at 45^0 relative to the direction of the polarizers.

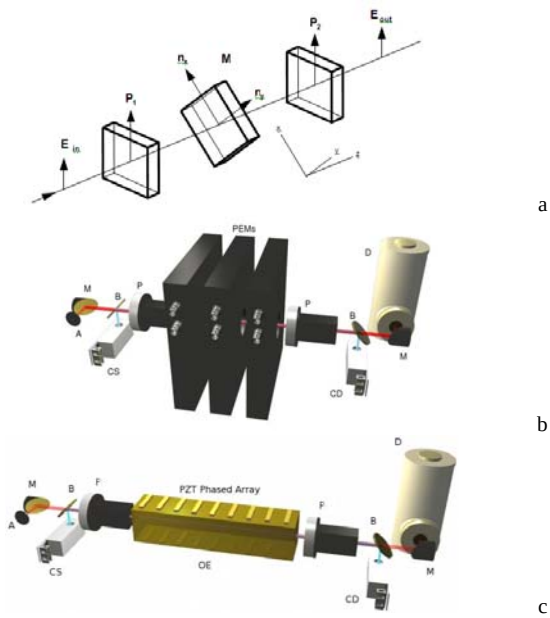

Fig. 1. PEM/FT spectrometry. (a) The basic birefringence interferometer. E_{in}, E_{out}—input and output electric vectors; M—birefringence modulator; n_x, n_y—principal indices of refraction of the birefringence modulator and the corresponding optical axes; and P_1, P_2—polarizers and their optical axes. If M is a single resonator PEM, then this is also a schematic illustration of a first-generation PEM/FT spectrometer. (b) Second-generation PEM/FTIR spectrometer prototype design based on actively tuned, stacked conventional PEMs: A—entrance aperture; D—detector; B—beam splitters; M—mirrors; CD—calibration detector; P—polarizers; CS—calibration source; PEMs—stacked photoelastic modulators. (c) Conceptual design of a third-generation PEM/FTIR spectrometer based on a bar-shaped virtual-stack PEM, driven by a phased array of PZTs. Components are as labeled in (b) and OE—optical element.

First generation PEM/FT spectrometers use single PEMs (or multiple PEMs without special driving and control systems characteristic of the second generation). Typically, a first generation PEM/FT spectrometer is mainly suited for low spectral resolution applications such as the analysis of molecular fluorescence (Buican, 1985).

Second generation PEM/FT spectrometers (Fig. 1b) address this limitation by (i) increasing PEM driving amplitude and (ii) stacking multiple PEMs. Both aspects of the technology require dedicated driving and control electronics that make the stacked PEMs operate in phase by actively and continuously tuning them to a common resonant frequency (Buican 2005, 2006). Because of the large number of optical interfaces in the PEM stack, the light throughput of these instruments is relatively low.

Third generation PEM/FT spectrometers (Fig. 1c) eliminate the high light loss associated with the many optical interfaces in the stack by replacing the latter with a "virtual" stack (VS): this is a solid bar of optical material that has only two optical interfaces but which, in terms of elastic wave propagation, behaves as if divided into stacked, isolated regions. The VS effect is created by a phased array (PA) of PZT drivers that are individually driven at well-determined relative amplitudes and phases. The resulting VSPA concept (Buican, 2008) is described below.

3. THE VSPA PHOTOELASTIC MODULATOR

3.1 Technical Context

It was shown by Canit and Badoz (Canit and Badoz, 1983) that small, low-power piezoelectric transducers attached to the sides of a bar-shaped elastic solid excite stress-waves propagating along the long axis of the bar medium (Fig. 2). Canit and Badoz demonstrated stress amplitudes adequate to generate half-wave retardation in light propagating perpendicular to the bar by inducing a standing elastic wave along the bar's length, rather than across the medium as is the case in Kemp-type photoelastic modulators (Kemp, 1969). The Canit and Badoz (C&B)

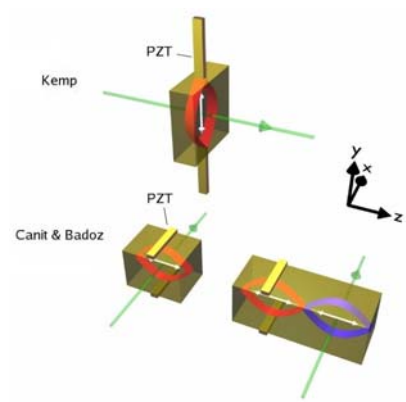

Fig. 2. Two important PEM designs. In the Kemp design (top), a fundamental mode standing elastic wave is set up perpendicular to the direction of the polarization-modulated light beam, and the PZT oscillations are collinear with the direction of the standing wave. (Standing elastic waves are shown here by ribbon-like representations of their amplitude envelopes; white double-ended arrows represent the direction of propagation of the elastic waves; and light beams are represented by green arrows.) The C&B design (bottom) is also based on standing elastic waves perpendicular to the direction of the light beam, but with PZTs mounted perpendicular to the standing wave. For longer bars (bottom right), the driving frequency is tuned to an overtone of the axial resonance. In this case, adjacent maxima (antinodes) of the standing wave have opposite phase (represented here by the red and purple colors of the amplitude envelopes).

design dispenses with the need for PZTs and optical elements to be finely tuned to a common resonant frequency; this simplifies the manufacturing process and reduces manufacturing cost. The ceramic non-resonant PZTs used in the C&B design typically require the use of a hard adhesive for good mechanical coupling, which can give rise to static stresses and thus to parasitic static birefringence. By exciting overtones in longer bars (Fig.2, bottom right), Canit and Badoz showed that the light beam can be

moved away from the PZTs and the associated static birefringence.

The C&B PEM design is interesting because its retardation amplitude scales with bar length and number of attached PZTs. This relationship is the consequence of the PZTs being mounted along the standing wave rather than at its ends, as in the Kemp design. Consequently, mechanical power can be injected into the optical element at each antinode and, except for losses due to attenuation, it eventually reaches the light beam and contributes to the local birefringence amplitude. The limitation of the design comes from the fact that the length of the optical path—one of the transverse dimensions of the bar—does not change as the length of the bar and number of PZTs increase.

The VSPA concept preserves the use of an elastic standing wave along the length of a bar-shaped optical element and of an array of PZTs placed along that wave. However, instead of using the end surfaces of the bar to define mechanical resonance, we use active control of the individual PZT amplitude and phase in order to isolate adjacent antinodes and drive them all in phase. This allows us to have an optical path that is coaxial with the elastic standing waves. Consequently, in a VSPA device, the optical path length and total retardation amplitude scale with bar length while the local stress amplitude does not.

3.2 Phased Arrays of PZTs

We introduce the conceptual framework behind the VSPA technology by means of a simple scalar 1-D model of elastic wave excitation and propagation in a bar-shaped optical element with attached PZTs. We represent the latter by point sources. The simple model also assumes that the stress wave propagates along one of the principal axes of the stress tensor; that the other two axes do not change direction over the domain of propagation of the elastic waves; and that the propagation medium at equilibrium is isotropic. Consequently, the principal axes of stress, stress-induced dielectric, and refractive index, tensors coincide (Born and Wolf, 1970) and both stress and induced birefringence can be treated as scalars that are proportional to each other. Fig. 3a shows a point source

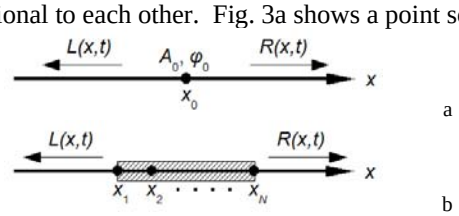

Fig. 3. (a) A point source at $x = x_0$ generates a local oscillation of amplitude A_0 and phase φ_0 which propagates to the left and right as waves *L(x,t)* and *R(x,t)*, respectively. (b) A set of *N* point sources contained within a finite interval and the waves *L(x,t)* and *R(x,t)* propagating outside the interval.

at x_0 which generates a stress (and associated birefringence) wave that propagates along the x axis and generates a local oscillation of amplitude $A_0(x)$, phase $\phi_0(x)$, and angular frequency ω. If the attenuation coefficient in the medium is β, waves propagating to the left and right of the source are given by $L(x,t) = \mathbf{A}_0 e^{i(\omega t + \boldsymbol{\kappa}(x - x_0))}$ and $R(x,t) = \mathbf{A}_0 e^{i(\omega t - \boldsymbol{\kappa}(x - x_0))}$, where $\mathbf{A}_0 = A_0 e^{i\phi_0}$ is the complex amplitude describing the oscillations at the source; and $\boldsymbol{\kappa}$ is the complex wavenumber $\boldsymbol{\kappa} = k - i\beta$, where $k = 2\pi/\lambda$ is the (real) wavenumber.

Fig. 3b shows a set of *N* point sources at $x_1 < x_2 < ... < x_N$ and oscillating with the same angular frequency ω and generating *N* sets of waves having amplitudes and phases A_j and ϕ_j at their respective sources. The sources are contained within a finite interval along the x axis, with *L(x,t)* and *R(x,t)* being, respectively, the waves propagating to the left and to the right of that interval. The left- and right-propagating waves are given by

$$L(x,t) = \left(\sum_{j=1}^{N} \mathbf{A}_j e^{-i\boldsymbol{\kappa} x_j} \right) e^{i(\omega t + \boldsymbol{\kappa} x)} \quad \text{and} \tag{1a}$$

$$R(x,t) = \left(\sum_{j=1}^{N} \mathbf{A}_j e^{i\boldsymbol{\kappa} x_j} \right) e^{i(\omega t - \boldsymbol{\kappa} x)} . \tag{1b}$$

The complex amplitudes of the two waves are seen to be essentially the Fourier transforms of the spatial distribution of sources, evaluated at $\pm\boldsymbol{\kappa}$. Thus, the amplitudes of the two waves are constant outside the source interval, except for the effect of attenuation in the medium. Consequently, if the amplitude of one of these waves vanishes on the boundary of the source interval, than its amplitude is zero anywhere outside the boundary and the purely geometric boundary point where the amplitude vanishes behaves like a mirror for the waves generated by the set of sources.

3.3 Active Reflectors

The waves propagating out of the source interval vanish if the wave complex amplitudes in Equations (1a) and (1b) vanish, $\sum_{j=1}^{N} \mathbf{A}_j e^{-i\boldsymbol{\kappa} x_j} = 0$ and $\sum_{j=1}^{N} \mathbf{A}_j e^{i\boldsymbol{\kappa} x_j} = 0$. The above equations are thus the wave cancellation conditions. If only one of these conditions is satisfied, then there is no wave propagation on the corresponding side of the source interval. The above equations each have nontrivial solutions for $N \geq 2$; in the simplest case, $N = 2$, one source can always be driven so as to cancel the wave arriving from the other. In this one-sided wave confinement, the cancelling source behaves as a virtual, active, reflector. The complex amplitudes for the virtual reflectors at x_1 and x_N (Fig. 3b) can easily be obtained by solving the wave cancellation equations for $\mathbf{A}_1$ and $\mathbf{A}_N$ respectively. These solutions, which depend in general on the posi-

tions of all sources, directly provide a global, open-loop approach to driving an active reflector. This can be quite onerous in terms of sensors and data processing requirements and thus impractical. However, the existence of a nontrivial solution to each complex amplitude equation makes possible a local approach to driving an active reflector, in which a local sensor or small set of sensors, together with a closed-loop controller, keep the wave amplitude at the active reflector at a certain acceptable error level. Interestingly, this approach to noise cancellation dates back to the 1930s (Lueg, 1934; see also Tokhi and Veres, 2002).

An active reflector can also be used as an isolator that separates two 1-D domains and prevents interactions between them through the cross-propagation of waves. As before, consider a set of M point sources to the left of the source to be used as isolator, positioned at x_{lj} such that $x_{l1} < x_{l2} < ... < x_{lM}$ (Fig. 4) and generating M sets of waves

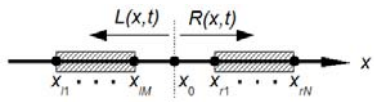

Fig. 4. If driven with the right phase and amplitude (see text), the point source at x_0 can block the propagation of waves from one side to the other and thus effectively isolate the two sets of sources.

with amplitudes and phases A_{lj} and ϕ_{lj} at their respective sources. Similarly, consider a set of N point sources to the right of the isolator, and use corresponding parameters having the index "r" instead of "l". From the wave cancellation equations, the waves generated by the sources to the right of the isolator do not propagate through it ($L(x,t)\equiv 0$ in Fig. 4) if the isolator source is driven with the complex amplitude $\mathbf{A}_r$ given by $\mathbf{A}_r = -\sum_{j=1}^{N} \mathbf{A}_{rj} e^{-i\boldsymbol{\kappa}(x_{rj}-x_0))}$, where x_0 is the position of the isolator source. Similarly, the complex amplitude for which the isolator blocks the propagation of the waves generated by the sources to its left ($R(x,t)\equiv 0$ in Fig. 4), $\mathbf{A}_l = -\sum_{j=1}^{M} \mathbf{A}_{lj} e^{i\boldsymbol{\kappa}(x_{lj}-x_0))}$. Under the assumption of linearity, driving the isolator with a complex amplitude equal to the sum $\mathbf{A}_0 = \mathbf{A}_r + \mathbf{A}_l$ will isolate the two sets of sources. (See Fig. 5; also note the simple example of active isolator shown in Fig. A2c of the Appendix.)

Fig. 5 shows how adjacent standing wave antinodes can be decoupled by means of an active isolator. In a thought experiment, two C&B fundamental-frequency PEMs are physically stacked (top right) and then brought together until they fuse (center right) and form one single bar of twice the original resonator length. This is similar to a first-overtone C&B PEM (Canit and Badoz, 1983), in which the interfering elastic waves propagate through the central node and thus cause the two antinodes to oscillate with opposite phase. By adding a node driver (bottom right) oscillating with the appropriate relative amplitude and phase, the two antinodes become independent again and can be driven in phase just like the separate PEMs in the physical stack (top right). Thus, the bar-shaped device in the bottom-right diagram can be regarded as a "virtual"

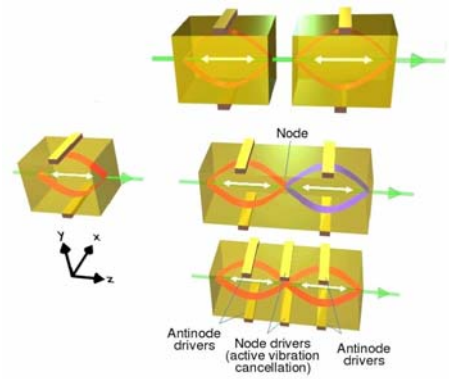

Fig.5. Conceptual path from a stack of PEMs to a Virtual-Stack PEM. Fundamental-mode C&B PEMs (left) can be physically stacked (top right) to increase total retardation amplitude, but at the cost of reduced light throughput because of reflection losses at the multiple optical interfaces. If the PEMs are brought into contact with each other so as to fuse into a single bar-shaped PEM (center right), additional light losses are eliminated but phase reversal at the central node causes the retardations in adjacent antinodes to cancel each other out. The addition of a "node driver" (bottom right) and active vibration cancellation isolates the adjacent antinodes which can now oscillate in phase. (See Fig. A2c for the numerical model of a similar configuration.)

stack driven by the phased array consisting of one node and two antinode drivers—the simplest example of a VSPA PEM.

3.4 Active Resonance Cells

If both wave amplitudes in Equations (1a) and (1b) vanish, there is active confinement of the waves within the source interval. A nontrivial solution always exists for $N \geq 3$. In the simplest case, $N = 3$ (Fig. 6, center), the

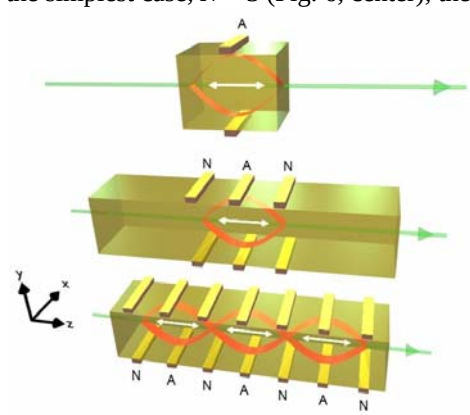

Fig. 6. Alternative conceptual path from a C&B PEM to a Virtual-Stack PEM. The equivalent of a fundamental-mode C&B PEM (top) can be implemented by means of an ARC in a bar-shaped optical element (center) (see also Fig. A2). Adjacent ARCs can share node drivers and a virtual stack of C&B-like PEMs can be implemented within a bar (see also Fig. A2c). (A—antinode driver; N—node driver. PZT drivers directly above each other are of the same type.)

two outside sources can be seen as actively confining a standing wave inside a virtual resonator. The standing wave appears to be driven by the middle source. For this reason, we refer to the two outside sources in this configuration as "node drivers"—they are placed at nodal points of the confined standing wave—and to the middle source as an "antinode driver", even though it need not be positioned exactly at a maximum of the wave amplitude. In reality, all three sources drive the confined standing wave.

For N=3, the optical medium and PZT driver array shown in Fig. 6 (center) form a "virtual" resonator that, without being bounded by physical discontinuities, behaves like the physical resonator shown in Fig. 6 (top) in terms of wave confinement. Satisfying both equations for the complex amplitudes means keeping the driving amplitudes and phases of the PZTs in certain relationships—the PZTs, together with their drive and control electronics, thus form a phased array. This phased array and the medium in which it excites elastic waves form what we call an Active Resonance Cell (ARC).

The lack of physical discontinuities in the ARC means that the propagation of optical waves along the optical axis of the device is not affected by scattering and absorption losses normally caused by such discontinuities. This is a fundamental advantage if achieving high retardation amplitudes requires the use of multiple resonators.

The effectiveness of an ARC is described by its effective stress amplitude (see the Appendix). The value of the effective amplitude is given for each of the examples shown in the Appendix. These values illustrate the fact that local stresses and birefringences add up constructively along an ARC's optical path and yield a high retardation amplitude. This is due to the essentially standing nature of the waves inside the ARCs, as well as to the absence of phase reversal at node drivers (isolators).

ARCs are robust. As the examples in the Appendix show (Fig. A2), wave confinement can be established even when the geometric and elastic wave propagation parameters are far removed from those required in a physical resonator. The effective stress amplitudes also remain high under such adverse conditions. Thus, both manufacturing variability and thermal effects can be easily compensated for electronically during operation by adjusting PZT amplitudes and phases.

4. MODELING AND COMPUTATION

4.1 Finite Element Modeling

The Finite Element Method (FEM) (see Pepper and Heinrich, 2006, for a good introduction to FEM) is a numerical technique for solving partial differential equations by discretizing their spatial domain into a mesh of small but arbitrarily shaped regions (finite elements). This results in matrix equations that relate the input at certain points (nodes) in the elements to outputs at the same points. A short history of the method can be found in Pepper and Heinrich (Pepper and Heinrich, 2006). Several well-established commercial packages based on FEM algorithms are available. For this work, we chose COMSOL Multiphysics (COMSOL, 2006) because of its ease of use and flexibility in incorporating and integrating models for a multitude of interacting physical phenomena.

The first published structural mechanics computer modeling of PEMs that we are aware of came from Canit and coworkers (Yang et al., 1995), who used a commercial FEM package to study the longitudinal elastic eigenmodes of their bar-shaped PEMs. Figures 7a and 7b show plots of the first two eigenmodes corresponding to C&M PEM operation. These plots were generated as part of our own survey of bar eigenmodes.

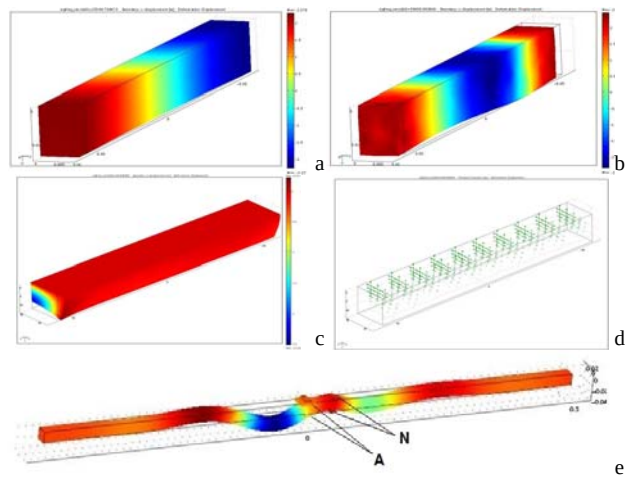

Fig. 7. COMSOL models of the bar-shaped PEM. First (a) and second (b) eigenmodes of a rectangular bar (see the text for details); An important higher eigenmode of the bar: boundary deformation and color-coded vertical displacement (c) and principal strain vectors (d); Virtual reflector effect showing a vertically polarized shear wave preferentially propagating leftwards (A—antinode driver PZTs; N—node driver PZTs). The eigenmode illustrations show only a quarter of the bar (lower right quadrant of the cross-section) which is assumed to be symmetrical.

The C&B-type eigenmodes are dominated by longitudinal (compression) waves that are reflected at the bar's ends. As can be gleaned from Fig. 7a and Fig. 7b, these are accompanied by transverse compression that is the same in both transverse directions and therefore does not result in significant birefringence in a transverse cross-section of the bar. Consequently, light traveling along the length of the bar as in a VSPA PEM does not record significant retardation between the two directions of polarization, while light traveling as in a C&B PEM does.

At the other extreme, a longitudinally nonpropagating mode (Fig. 7c) similar to that used in octagonal Kemp-style PEMs (Hinds Inc., Hillsboro, Oregon) can be established (Fig. 2, top) by reflection of compression waves propagating perpendicular to the length of the bar. As in the conventional Kemp design, this requires precise grinding of the side surfaces, which furthermore must apply to

the full length of the bar. This is, however, a highly effective way of generating high birefringence along the length of the bar since the stress and refractive index tensors have the eigenvectors for the highest and lowest eigenvalues in the transverse cross-section of the bar (see Fig. 7 d for the corresponding strain eigenvectors). Furthermore, this high birefringence can extend to most of the length of the bar.

We also use COMSOL Multiphysics to generate time-dependent simulations showing the propagation of PZT-generated elastic waves. For example, Fig. 7e shows an active mirror (node driver) as described in Section 3 that reflects (with some losses) a pure shear waves propagating from a source (antinode driver) to the left of the reflector. This is important because the compromise between extreme manufacturing precision and low PEM performance can be found among the many propagating modes characteristic of the solid bar (Auld, 1990) in conjunction with VSPA driving and control technology, and these modes generally exhibit significant shear.

4.2 Computation

We are currently using both free open-source and commercial off-the-shelf (COTS) finite element modeling (FEM) software to create comprehensive multiphysics models of the VSPA PEM optical element. The models are developed and tested on HERD-0, a small in-house PC cluster (Fig. 8).

Fig. 8. The HERD-0 PC cluster assembled at SEA LLC for physical modeling work. Each of the nine nodes has a dual core Athlon 64 processor and 3 GB of RAM. The nine PCs are connected by a private Gigabit Ethernet network and are powered by uninterruptible power supplies. HERD-0 exceeded 56 Gflops/s.

The HERD-0 cluster uses many open source software packages such as the Rocks cluster management system (Papadopoulos et al., 2001) and the Trilinos library of object-oriented linear algebra tools and solvers (Heroux et al., 2003). The commercial COMSOL Multiphysics package (COMSOL AB, 2006) is installed on the cluster's head node and is used for multiphysics modeling of the interacting mechanical, thermal and optical processes in the PEM bar and PZT array.

An interface between COMSOL and the Trilinos solvers running in parallel on the cluster was developed in house; this interface allows the problem set up in COMSOL to be transferred, via COMSOL Script (COMSOL AB, 2006), Java/JNI and C++ code, to the appropriate cluster-based Trilinos solvers, and the results transferred back to COMSOL for postprocessing and display. A large PC cluster at the Army Research Laboratory (ARL) Major Shared Resource Center (MSRC), Aberdeen Proving Ground, MD, will be used for production runs once the FEM model has been debugged and tested on the local cluster.

5. PRELIMINARY DESIGN CONSIDERATIONS

The diagrams in Figures 1, 5 and 6 illustrate the use of two nonresonant ceramic PZTs similar to the ones used by Canit et al. (Fig. 2 and Canit and Badoz, 1983; Yang et al., 1995) for each node and antinode driver. These PZTs are placed on opposite faces of the bar-shaped optical element. Additional configurations consisting of four or more PZTs per node or antinode driver are under consideration and seem to be required for exciting vibration modes with high associated birefringence (see Figures 7c and 7d for an example of such a mode). The driving and control electronics for the phased array of PZTs deployed along the length of the bar may need to be supplemented by additional phase controls between PZT on different faces of the bar. These and other recent work on the efficient driving of the phased array will be described elsewhere.

The use of relatively inexpensive nonresonant ceramic PZTs will result in a considerable reduction in the cost of high retardation amplitude PEMs. The elimination of the numerous optical interfaces present in a PEM stack will also considerably reduce manufacturing costs. Furthermore, the use of low-profile PZTs with a large contact area will likely result in rugged designs suitable for use in the field and on mobile platforms such as combat vehicles and helicopters.

6. DEFENSE APPLICATIONS

We have previously discussed (Buican and Carrieri, 2004; Buican and Carrieri, 2006) a range of explosive trace detection and CB defense applications that are made possible by, or can benefit considerably from, the use of PEM/FT spectrometers. These applications range from novel spectrometric techniques for the detection and recognition of surface contaminants (Buican and Carrieri, 2006; Carrieri et al, 1999) to panoramic hyperspectral IR imagers for detecting and tracking chemical clouds (Carrieri, 2003).

Any application that requires the speed, broadband characteristics and light throughput of a PEM/FT spectrometer would benefit even more from the third-generation VSPA PEM technology. As previously discussed, the latter improves on the light throughput of stacked-PEM instruments while allowing for more rugged and compact instrument designs that are better suited for field use. In fact, because of their inherent advantages over older approaches, VSPA PEMs will likely be the common enabling technical element for these novel detection technologies. As these techniques are strategically important by virtue of their likely impact in combat zones and in homeland security, VSPA PEMs themselves become the nexus of a strategic advantage.

We briefly review in what follows three strategically important spectral techniques for use in explosive trace detection and CB defense and for which VSPA will likely turn out to be the enabling technology.

We described multivariate PEM/FT spectrometry, M-PEMS (Buican and Carrieri, 2006), as an active spectral technique that provides correlated excitation, emission and lifetime fluorescence spectra. These three-dimensional spectra are inherently more likely to provide the basis for reliable discrimination than regular spectral data. Furthermore, multivariate spectrometers could be used in standoff configurations to analyze small sample volumes, including small volumes of surface contaminants. And, when used in conjunction with ultrashort pulse lasers, multivariate spectrometers could analyze trace surface contaminants of low vapor pressure and/or low intrinsic fluorescence.

Thermal luminescence (TL) is a technology aimed at solving the standoff detection problem of contaminated water reservoirs and terrestrial surfaces (Carrieri et al., 1999). In TL, the energy of an irradiating beam is absorbed into the target material; by scanning the irradiated surface, the PEM/FTIR spectrometer produces high-speed interferograms that are transformed into graybody spectra of the TL. During beam irradiation, a thermal gradient is produced at the target surface; inside the thermal nonequilibrium heating period, a detection window of opportunity develops and the absorption bands of contaminant are revealed. These bands are quite strong provided the graybody envelope shifts at maximum rate (i.e., the maximum gradient condition), which requires high interferogram acquisition rates that can only be provided by PEM/FTIR spectrometers.

PANSPEC (Panoramic Infrared-Imaging Spectroradiometer) is a computer-optimized spectroradiometer design for monitoring a panoramic infrared environment for the presence of chemical clouds, and for tracking such clouds (Carrieri, 1997a, 1997b, 2003). It combines imaging PEM/FTIR and photopolarimeter technologies and integrates a wide-angle camera in forming a unified passive imaging remote sensor and active laser beacon system. PANSPEC provide a standoff detection capability for disseminated chemical weapons; specifically, (1) detection of gaseous chemical warfare agents in the atmosphere to a range of approximately 50 km (a figure of merit for prototype construction); (2) tracking of the targeted hazardous cloud mass over a panoramic field of view; and (3) omnidirectional communications of cloud presence and heading by means of an encrypted laser beam carrier, projected into the exact panorama from which imaging is done.

CONCLUSIONS

The VSPA concept shows considerable promise as the basis for high retardation amplitude PEMs for use in ultra-high performance FT spectrometers. While additional modeling and experimental work is required in order to refine the concept and demonstrate it experimentally, we believe that VSPA PEM/FT spectrometry has the potential to become the enabling technology for fast, sensitive, and reliable optical detection and identification of specific chemical and biological agents and contaminants.

APPENDIX

We define the effective amplitude and phase for the parameters of interest—in this case, stress and stress-induced birefringence—as the (real) amplitude and phase of the average value of the complex amplitude over the optical path through the ARC or well-defined portion thereof, $\mathbf{A}_{eff} = A_{eff} e^{i\varphi_{eff}} = \frac{1}{\Lambda}\int_{\Lambda} \mathbf{A}(x,t)dx$, where Λ is the interval of interest inside the ARC and $\mathbf{A}(x,t)$ is the complex amplitude of the oscillations $w(x,t)$ inside the interval, $w(x,t) = \mathbf{A}(x,t)e^{i\omega t}$.

The examples given below show the amplitude and phase distributions for ARCs with various geometries and elastic wave propagation properties. The antinode driver is positioned at the origin. The wave's peak amplitude is set to one amplitude unit and its phase at the origin to

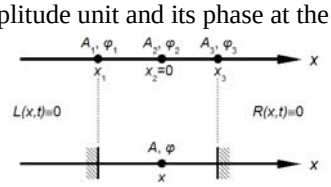

Fig. A1. The three sources forming an ARC (top) in the examples shown in Fig. A2 and the equivalent conventional resonator bounded by two reflecting surfaces (bottom). Of course, the conventional resonator adequately functions only for reflector separations that are integer multiples of $\lambda/2$. The node drivers are situated at x_1, x_3, and the antinode driver is at the origin.

zero. Please note that the waves in all the examples below are fully contained within the ARC despite large deviations from standing-wave conditions.

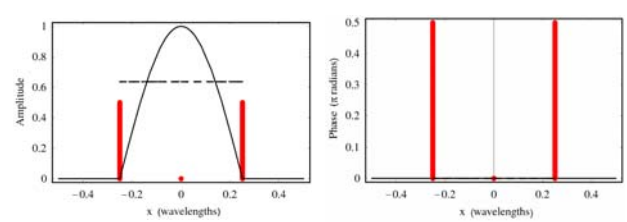

(a) $x_1 = -0.25$, $x_2 = 0$, $x_3 = 0.25$; $\beta = 0$; $A_{eff} = 0.636$

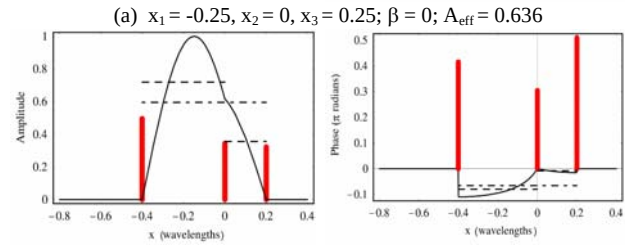

(b) $x_1 = -0.4$, $x_2 = 0$, $x_3 = 0.2$; $\beta = 0.5$; $A_{eff} = 0.596$

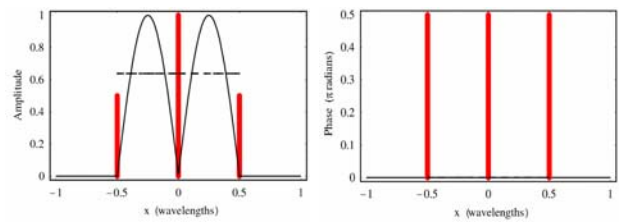

(c) $x_1 = -0.5$, $x_2 = 0$, $x_3 = 0.5$; $\beta = 0$; $A_{eff} = 0.636$

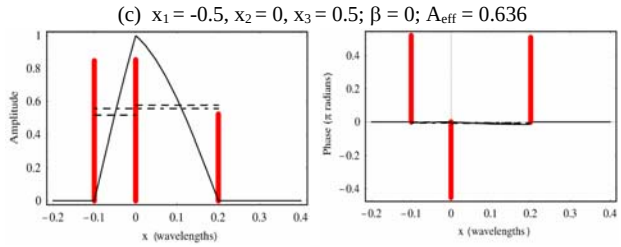

(d) $x_1 = -0.1$, $x_2 = 0$, $x_3 = 0.2$; $\beta = 0.5$; Aeff = 0.557

Fig. A2. Each row of drawings shows the amplitude (left) and phase (right) profile for an ARC (black lines). The red vertical bars show respectively the values of the amplitudes and phases for the three sources of the ARC. The dashed lines show respectively the effective amplitude and phase for each ARC interval, and the point-dashed line shows the values for the entire ARC. The data were normalized for unit peak wave amplitude and for zero wave phase at the origin. For each example we give the positions of the three sources (in wavelengths); the attenuation coefficient β (per wavelength); and the effective amplitude over the entire ARC. (a) The node-antinode separation is $\lambda/4$ and there is no attenuation; this corresponds to the fundamental resonance and is a special case in that the antinode source amplitude is zero and the ARC is reduced to only two sources. The effective amplitude is 0.636, the characteristic value for a conventional standing wave between two adjacent nodes. The node drivers are characteristically ahead of the wave phase at the origin by $\pi/2$. (b) A highly nonsymmetric ARC with high attenuation; although there is some change in wave phase within the ARC, the effective amplitude is still high. (c) The node-antinode separation is $\lambda/2$ and there is no attenuation; each half of the ARC becomes itself an ARC as in (a) and the antinode driver can be regarded as an isolator. (d) A highly nonsymmetric ARC that is very far from standing-wave geometry. Adversity notwithstanding, the effective amplitude is still 87.6% of the value for the ideal standing wave in (a).

ACKNOWLEDGMENTS

This work was supported in part by the U.S. Army RDECOM Edgewood Chemical Biological Center under the auspices of a Department of the Army Innovative Research grant. It was also supported in part by a grant of computer time from the DOD High Performance Computing Modernization Program at the ARL MSRC.

REFERENCES

Auld, B.A., 1990: *Acoustic Fields and Waves in Solids*, 2nd ed., Krieger Publishing Company, Malabar, Florida.

Born, M. and Wolf, E., 1970: *Principles of Optics*, 3rd ed., §14.5.1, Pergamon Press, Oxford, UK.

Buican, T.N., 1985: Fourier Transform Flow Cytometry – The Interferometric Analysis of Emission Spectra from Individual Cells, *Proc. 11th Intl. Conf. of Analytical Cytology*, Hilton Head, SC, Intl. Soc. Analyt. Cytology.

Buican, T.N., 2005: Controlling Resonant Photoelastic Modulators. US Patent No. 6,970,271.

Buican, T.N., 2006: Birefringence Interferometers for Ultra-High-Speed FT Spectrometry and Hyperspectral Imaging: I. Dynamic Model of the Resonant Photoelastic Modulator, *J. Vib. Spec*. 42, 51-58.

Buican, T.N., 2008: High Retardation-Amplitude Photoelastic Modulator, US Patent pending.

Buican, T.N. and Carrieri, A.H., 2004: Ultra-High Speed Solid-State FTIR Spectroscopy and Applications for Chemical Defense, *24th Army Science Conference Proceedings*, http://handle.dtic.mil/100.2/ada431953.

Buican, T.N. and Carrieri, A.H., 2006: Multivariate PEM /FT Spectrometry: Intrinsic Data Fusion and Applications for IED and CB Defense. *25th Army Science Conference Proceedings, in Selected Topics in Electronics and Systems*, vol. 42, AP-11, World Scientific, Singapore.

Buican, T.N. and Martin, J.C., 1990: Method and Apparatus for Simultaneously Measuring a Plurality of Wavelenghts Present in Electromagnetic Radiation, US Patent No. 4,905,169.

Canit, J.C. and Badoz, J., 1983: New Design for a photoelastic modulator, *Appl. Opt*. 22, 592-594.

Carrieri, A. H., 2003: Chemical Imaging Sensor and Laser Beacon, *Appl. Opt.*, 42(15), 2772-2784.

Carrieri, A. H., Barditch, I., Owens, D. J., Talbard, M., Lim, P. I. and Roese, E. S. 1999: Thermal Luminescence Sensor for Ground Path Contamination Detection, *Appl. Opt*., 38(27), 5880-5886.

COMSOL AB, 2006: *COMSOL Multiphysics User's Guide*, COMSOL, Inc., Burlington, MA.

Heroux, M. et al., 2003: An Overview of Trilinos, Sandia Report 2003-2927, Sandia National Laboratories, Albuquerque, NM.

Kemp, J.C., 1969: Piezo-Optical Birefringence Modulators: New Use for a Long Known Effect, *J. Opt. Soc. Am*. 59, 950-954.

Lueg, P., 1934: Process of Silencing Sound Oscillations, US Patent No. 2,043,416.

Papadopoulos, P.M., Katz, M.J. and Bruno, G., 2001: NPACI Rocks: Tools and Techniques for Easily Deploying Manageable Linux Clusters, *Concurrency and Computation: Practice and Experience* Special Issue: Cluster 2001.

Pepper, D.W. and Heinrich, J.C., 2006: *The Finite Element Method*, 2nd ed., Taylor and Francis, New York, NY.

Tokhi, O. and Veres, S. (eds.), 2002: *Active Sound and Vibration Control: Theory and Applications*, IEE Control Engineering Series 62, The Institution of Electrical Engineers, London, UK.

Yang, D., Canit, J.C. and Gaignebet, E., 1995: Photoelastic Modulator: Polarization modulation and phase modulation, *J. Optics (Paris)* 26, 151-159.